Scientific Research Publishing

Open Journal of Composite Materials, 2026, 16(2), 59-72
https://www.scirp.org/journal/ojcm
ISSN Online: 2164-5655
ISSN Print: 2164-5612

Multiscale Investigation of Hydrogen Adsorption in Vacancy-Engineered CNCs: A Combined DFT and PHITS Monte Carlo Study

Mohammed Ahmed Al-Khateeb[1*], Ahlam El-Barbary[2]

[1]Physics Department, Faculty of Education and Science, Taiz University, Taiz, Yemen
[2]Department of Physical Sciences, Physics Division, College of Science, Jazan University, Jazan, Kingdom of Saudi Arabia
Email: *m_alkhateeb@taiz.edu.ye, ahla_eg@yahoo.co.uk

How to cite this paper: Al-Khateeb, M.A. and El-Barbary, A. (2026) Multiscale Investigation of Hydrogen Adsorption in Vacancy-Engineered CNCs: A Combined DFT and PHITS Monte Carlo Study. *Open Journal of Composite Materials*, **16**, 59-72.
https://doi.org/10.4236/ojcm.2026.162004

Received: January 8, 2026
Accepted: February 22, 2026
Published: February 25, 2026

Abstract

The rapid exhaustion of fossil fuel resources, coupled with increasing environmental degradation, has driven the pursuit of sustainable and clean energy carriers. Hydrogen, in particular, has attracted considerable attention as a potential alternative energy medium capable of addressing these challenges, while also aligning with the performance targets established by DOE. This study systematically investigates the synergistic effects of mono-vacancy engineering (V1 at the apex, V2 away from the apex) on the hydrogen adsorption properties of carbon nanocones (CNCs) across five disclination angles (60˚ - 300˚). First-principles DFT calculations (B3LYP/6-31G) reveal that the $C_{89}H_{10}$-V1-H^{S2} configuration at a 300˚ disclination angle possesses the most favorable adsorption energy of −4.95 eV, a peak dipole moment of 24.21 D, and a minimum energy gap of 0.02 eV. Complementary Monte Carlo simulations performed via PHITS 3.35 provide a macroscopic validation, demonstrating that these vacancy sites act as focal points for energy localization. The results indicate a maximum localized temperature rise of 34.8 K and an absorbed dose of 0.82 Gy. These findings confirm that vacancy-induced electronic modulation, combined with localized thermal excitation, significantly enhances the hydrogen storage potential of CNCs for irradiation-assisted applications.

Keywords

Mono-Vacancy, CNCs, Density Functional Theory, Hydrogen Storage, Surface Reactivity, PHITS Monte Carlo Simulation, Energy Deposition

1. Introduction

Nanomaterials have emerged as one of the most transformative innovations in

modern science and engineering, offering an extensive range of applications that span across electronics, energy storage, medicine, catalysis, and aerospace technologies. Their properties are uniquely defined by quantum confinement, pronounced surface-to-volume ratios, and tunable electronic structures, setting them apart from bulk forms. These features have enabled nanomaterials to play an increasingly significant role in the miniaturization and performance optimization of contemporary devices, from everyday consumer electronics to complex onboard satellite systems. As the demand for faster, lighter, and more energy-efficient technologies continues to rise, research in nanoscience and nanotechnology has intensified considerably over the past few decades [1]-[6].

The 1991 discovery of carbon nanotubes (CNTs) by Iijima [7] marked a turning point in the study of low dimensional carbon-based materials. Owing to their extraordinary electrical conductivity, exceptional tensile strength, high aspect ratio, and chemical stability, CNTs rapidly became the focus of extensive theoretical and experimental investigations. Their versatile properties have led to exploration in a wide variety of applications, including nanoscale transistors, hydrogen storage systems, biosensors, and composite materials. Following this discovery, researchers extended their attention to other related carbon nanostructures such as fullerenes, graphene, and carbon nanocones (CNCs), each possessing distinctive geometrical and electronic features [8]-[10].

Carbon nanocones, in particular, have drawn substantial interest due to their conical geometry, which introduces localized strain and curvature dependent properties that differ from those observed in CNTs. Despite their structural similarity to nanotubes, CNCs exhibit unique edge states, apex reactivity, and potential field-emission characteristics that make them attractive for applications in catalysis, energy storage, and nanoelectronics [11] [12]. More recently, attention has extended to carbon nanocones (CNCs), the conical analogues of CNTs, which combine many of their advantageous characteristics with unique geometrical features that offer new opportunities for nanoscale precision engineering [2] [13]-[20].

Parallel developments in hydrogen energy storage have intensified research into nanostructured carbon materials as potential hydrogen storage media. CNTs, graphene derivatives, and porous carbon frameworks are being studied for their ability to store hydrogen through physisorption and chemisorption, enabled by their high surface-to-volume ratios and adjustable pore architectures [21]-[32]. The hollow cylindrical morphology and low mass density of CNTs, in particular, support efficient hydrogen adsorption and release, processes that are highly sensitive to temperature and therefore controllable for practical applications [33]-[36]. Mechanistic studies have shown that hydrogen adsorption often begins with catalytic dissociation of H_2 molecules at metal nanoparticle sites residual from synthesis followed by the migration of atomic hydrogen onto the carbon substrate [37]-[41]. Such findings underscore the combined roles of catalytic impurities and nanoscale design in enhancing hydrogen uptake efficiency and optimizing material performance for clean energy storage.

This study bridges this gap by investigating the hydrogenation of mono-vacancy engineered CNCs (V1 at the apex and V2 distal to the apex) across five disclination angles (60˚ - 300˚). By employing a dual-methodological approach, we utilize Density Functional Theory (DFT) to resolve atomic-scale adsorption energetics and electronic reactivity (H^{S1}, H^{S2}, and H^{S3} sites), while simultaneously implementing Monte Carlo simulations via PHITS 3.35 to evaluate the macroscopic radiation-matter interactions and thermal responses [42]. This multiscale framework aims to elucidate the role of structural vacancies in governing both the chemical binding stability and the irradiation-assisted activation of hydrogen storage in CNC-based systems.

2. Materials and Methods

2.1. Computational Framework: DFT Analysis

Atomic-scale investigations were conducted using Density Functional Theory (DFT) as implemented in the Gaussian 09W package [43]. The B3LYP hybrid functional [44] [45] was employed in conjunction with the 6-31G basis set for all constituent atoms. Geometric models were constructed and analyzed using the Gauss View 5 interface [46]. The study focused on hydrogenated CNCs featuring mono-vacancy defects (V1 and V2) across disclination angles of 60˚, 120˚, 180˚, 240˚, and 300˚ (**Figure 1**). For each disclination angle, the atomic composition was uniquely determined by the topological construction of the truncated graphene cone followed by edge reconstruction and hydrogen passivation of all under-coordinated rim atoms. This procedure produces the parent stoichiometries shown in **Figure 1**, namely $C_{80}H_{20}$ for 60˚, $C_{92}H_{20}$ for 120˚, $C_{102}H_{18}$ for 180˚, $C_{94}H_{14}$ for 240˚, and $C_{90}H_{10}$ for 300˚, reflecting the systematic variation of rim length and

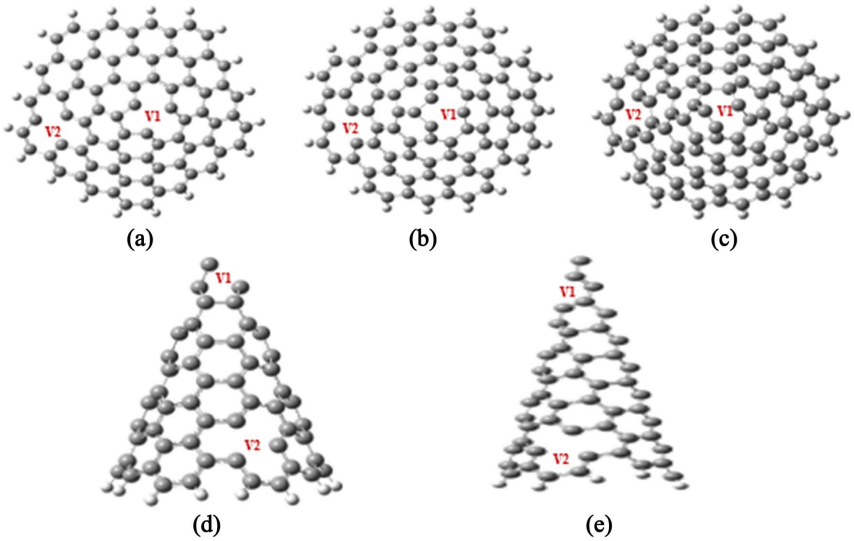

Figure 1. Schematic representation of mono-vacancy CNCs: (a) $C_{80}H_{20}$ with disclination angle 60˚, (b) $C_{92}H_{20}$ with disclination angle 120˚, (c) $C_{102}H_{18}$ with disclination angle 180˚, (d) $C_{94}H_{14}$ with disclination angle 240˚ and (e) $C_{90}H_{10}$ with disclination angle 300˚ (grey atoms are represented carbon atoms and white atoms are represented hydrogen atoms).

coordination number with increasing disclination. To eliminate edge-effect artifacts and ensure electronic stabilization, peripheral dangling bonds were saturated with hydrogen atoms. Mono-vacancy defects (V1 and V2) were then introduced by removing a single carbon atom from the optimized parent structures without modifying the hydrogen termination, yielding the defected systems illustrated in Figure 2, including $C_{79}H_{20}$-V1, $C_{79}H_{20}$-V2, $C_{89}H_{10}$-V1, and $C_{89}H_{10}$-V2. Geometry optimizations were performed without symmetry constraints, allowing for the complete relaxation of bond lengths and bond angles until stringent convergence criteria for energy and forces were satisfied. Adsorption energies (Eads), HOMO-LUMO gaps, and density of states (DOS) were systematically evaluated for three distinct sites (H^{S1}, H^{S2}, and H^{S3}) across varying cone sizes (Figure 2).

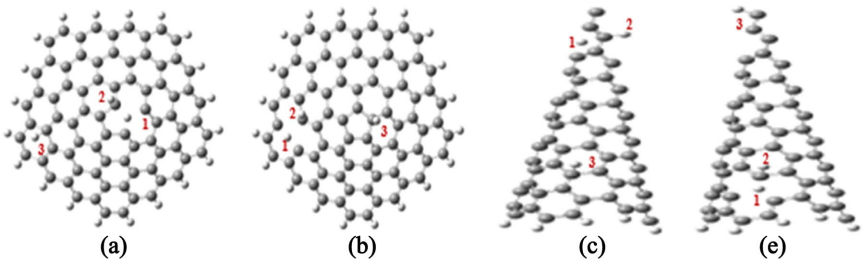

Figure 2. Optimized structures for hydrogenation sites 1-HS1, 2-HS2, 3-HS3 of mono-vacancy CNCs with disclination angle 60˚ for structures (a) $C_{79}H_{20}$-V1, (b) $C_{79}H_{20}$-V2, and with disclination angle 300˚ for structures (c) $C_{89}H_{10}$-V1, (d) $C_{89}H_{10}$-V2.

2.2. Macroscopic Simulation: PHITS 3.35 Implementation

To extend the analysis to macroscopic irradiation response and thermal behavior, Monte Carlo simulations were executed using the Particle and Heavy Ion Transport Code System (PHITS), version 3.35 [42] [47]. In these simulations, the CNC frameworks were irradiated by a monoenergetic proton beam with a kinetic energy of 10 MeV and electron beam with a kinetic energy of 1 MeV, selected to ensure effective coupling between the incident particles and the light-element lattice of carbon nanocones. This phase of the study aimed to quantify the energy deposition density, absorbed dose, and localized temperature rise (ΔT) within the CNC frameworks under irradiation. The chosen proton energy lies within the regime of high stopping power for carbon-based materials, allowing simultaneous treatment of ionization losses and elastic nuclear scattering, which is essential for capturing both electronic excitation and atomic-scale energy transfer. The simulation geometry mirrored the optimized DFT structures, accounting for the localized electronic environment induced by V1 and V2 vacancies. Incident particle interactions were modeled to assess how structural disclinations influence the interaction cross-section and energy dissipation pathways under 5 MeV proton irradiation. By integrating the microscopic binding energetics from DFT with the macroscopic energy deposition spectra from PHITS, a synergistic correlation was established to identify the most responsive configurations for irradiation-assisted hydrogen activation.

3. Results and Discussion

3.1. Hydrogen Adsorption Energetics and Electronic Structure

The adsorption behavior of a single hydrogen atom on mono-vacancy (V1 and V2) carbon nanocones (CNCs) was systematically examined at three hydrogenation sites (H^{S1}, H^{S2}, and H^{S3}), as shown in Figure 2. The calculated adsorption energies listed in Table 1, demonstrate that HS2 is consistently the most energetically favorable site. In all cases, V1-containing CNCs exhibit more negative adsorption energies than their V2 counterparts, indicating stronger thermodynamic stability when hydrogen atoms bind to carbon atoms adjacent to mono-vacancies. The most stable adsorption energies were determined to be −2.45 eV, −3.46 eV, −3.55 eV, −2.87 eV, and −4.95 eV at disclination angles of 60˚, 120˚, 180˚, 240˚, and 300˚, respectively, revealing that hydrogen binding strength increases with cone size and disclination angle. This trend is consistent with previous theoretical reports [1] [48], with the $C_{89}H_{10}$-H^{S2}-V1 configuration at 300˚ identified as the most stable system (−4.95 eV). Correspondingly, the electronic band gaps of hydrogenated mono-vacancy CNCs, summarized in Table 2, show that V1 systems consistently possess narrower gaps than V2 systems. The minimum and maximum band gaps were found to be 0.02 eV for $C_{89}H_{10}$-V1-H^{S2} at 300˚ and 0.08 eV for $C_{79}H_{20}$-V2-H^{S1} at 60˚, respectively, with the band gap decreasing as cone angle and size increase, in agreement with earlier studies [31]-[33]. As illustrated in Figure 3, the HOMO of hydrogenated $C_{89}H_{10}$-V1 at 300˚ is highly localized around the vacancy and neighboring carbon atoms, while the LUMO extends over the conical surface toward the defect region, facilitating charge transfer through the vacancy site. The resulting reduction in the HOMO-LUMO gap enhances electronic conductivity and surface reactivity, providing a coherent electronic explanation for the observed adsorption trends and confirming the critical role of mono-vacancy engineering in improving the hydrogen storage potential of CNCs.

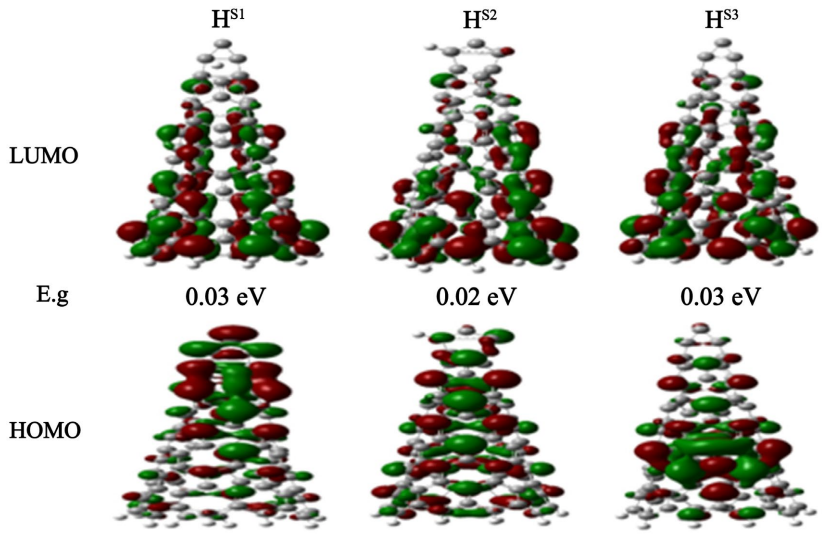

Figure 3. The molecular orbital of HOMOs, LUMOs for hydrogenated mono-vacancy $C_{89}H_{10}$-V1 with disclination angle 300˚.

Table 1. The configuration structures and the adsorption energy of hydrogenated mono-vacancy (V1 and V2) CNCs for disclination angles 60˚, 120˚, 180˚, 240˚, and 300˚. All energies are given by eV.

	Angle 60˚		Angle 120˚		Angle 180˚		Angle 240˚		Angle 300˚	
	Structures	E_{ads}^{H}	Structures	E_{ads}^{H}	Structures	E_{ads}^{H}	Structures	E_{ads}^{H}	Structures	E_{ads}^{H}
V1	$C_{79}H_{20}$-H^{S1}	−1.35	$C_{91}H_{20}$-H^{S1}	−2.40	$C_{101}H_{18}$-H^{S1}	−1.83	$C_{93}H_{14}$-H^{S1}	−2.87	$C_{89}H_{10}$-H^{S1}	−3.78
	$C_{79}H_{20}$-H^{S2}	−2.45	$C_{91}H_{20}$-H^{S2}	−3.46	$C_{101}H_{18}$-H^{S2}	−3.55	$C_{93}H_{14}$-H^{S2}	−2.02	$C_{89}H_{10}$-H^{S2}	−4. 95
	$C_{79}H_{20}$-H^{S3}	−1.82	$C_{91}H_{20}$-H^{S3}	−0.34	$C_{101}H_{18}$-H^{S3}	−2.04	$C_{93}H_{14}$-H^{S3}	−2.25	$C_{89}H_{10}$-H^{S3}	−3.20
V2	$C_{79}H_{20}$-H^{S1}	−0.63	$C_{91}H_{20}$-H^{S1}	−2.49	$C_{101}H_{18}$-H^{S1}	−1.63	$C_{93}H_{14}$-H^{S1}	−1.07	$C_{89}H_{10}$-H^{S1}	−1.10
	$C_{79}H_{20}$-H^{S2}	−1.80	$C_{91}H_{20}$-H^{S2}	−1.34	$C_{101}H_{18}$-H^{S2}	−2.91	$C_{93}H_{14}$-H^{S2}	−1.75	$C_{89}H_{10}$-H^{S2}	−2.80
	$C_{79}H_{20}$-H^{S3}	−0.39	$C_{91}H_{20}$-H^{S3}	−1.21	$C_{101}H_{18}$-H^{S3}	−0.47	$C_{93}H_{14}$-H^{S3}	−2.08	$C_{89}H_{10}$-H^{S3}	−1.64

Table 2. The configuration structures and the energy gap of hydrogenated mono-vacancy (V1 and V2) CNCs for disclination angles 60˚, 120˚, 180˚, 240˚, and 300˚. All energies are given by eV.

	Angle 60˚		Angle 120˚		Angle 180˚		Angle 240˚		Angle 300˚	
	Structures	Eg	Structures	Eg	Structures	Eg	Structures	Eg	Structures	Eg
V1	$C_{79}H_{20}$-H^{S1}	0.06	$C_{91}H_{20}$-H^{S1}	0.04	$C_{101}H_{18}$-H^{S1}	0.05	$C_{93}H_{14}$-H^{S1}	0.03	$C_{89}H_{10}$-H^{S1}	0.03
	$C_{79}H_{20}$-H^{S2}	0.04	$C_{91}H_{20}$-H^{S2}	0.03	$C_{101}H_{18}$-H^{S2}	0.05	$C_{93}H_{14}$-H^{S2}	0.03	$C_{89}H_{10}$-H^{S2}	0.02
	$C_{79}H_{20}$-H^{S3}	0.04	$C_{91}H_{20}$-H^{S3}	0.03	$C_{101}H_{18}$-H^{S3}	0.04	$C_{93}H_{14}$-H^{S3}	0.03	$C_{89}H_{10}$-H^{S3}	0.03
V2	$C_{79}H_{20}$-H^{S1}	0.08	$C_{91}H_{20}$-H^{S1}	0.04	$C_{101}H_{18}$-H^{S1}	0.05	$C_{93}H_{14}$-H^{S1}	0.04	$C_{89}H_{10}$-H^{S1}	0.05
	$C_{79}H_{20}$-H^{S2}	0.06	$C_{91}H_{20}$-H^{S2}	0.03	$C_{101}H_{18}$-H^{S2}	0.06	$C_{93}H_{14}$-H^{S2}	0.03	$C_{89}H_{10}$-H^{S2}	0.04
	$C_{79}H_{20}$-H^{S3}	0.04	$C_{91}H_{20}$-H^{S3}	0.04	$C_{101}H_{18}$-H^{S3}	0.04	$C_{93}H_{14}$-H^{S3}	0.03	$C_{89}H_{10}$-H^{S3}	0.04

3.2. Surface Reactivity and Density of States Characteristics

The surface reactivity of hydrogenated mono-vacancy (V1 and V2) carbon nanocones (CNCs) with different disclination angles (n × 60˚, n = 1 - 5) and cone sizes was evaluated using dipole moments as reliable reactivity indicators [49] [50], as summarized in Table 3. In general, higher dipole moments correspond to enhanced surface reactivity, whereas lower values indicate improved structural stability. Mono-hydrogenation was examined at three adsorption sites (H^{S1}, H^{S2}, and H^{S3}), revealing a strong dependence on both adsorption site and angular configuration. Among all systems, the $C_{89}H_{10}$-V1-H^{S2} structure at a 300˚ disclination angle exhibits the highest dipole moment (~24.21 D), indicating pronounced surface reactivity, while the $C_{79}H_{20}$-V2-H^{S3} configuration at 60˚ shows the lowest value (~5.42 D), reflecting enhanced stability. Overall, surface reactivity increases with increasing cone angle and cone size, consistent with experimental observations reporting hydrogen storage capacities exceeding 7 wt% in highly curved nanostructures [51].

The corresponding electronic response is elucidated through density of states (DOS) analysis shown in Figure 4. For the $C_{79}H_{20}$-V1 structure at a 60˚ disclination angle, distinct defect-induced states appear near the Fermi level and are significantly reduced upon hydrogen adsorption, indicating partial defect pas-

sivation and improved electronic stability. In contrast, the $C_{89}H_{10}$-V1 structure at 300˚ exhibits broader DOS features and a reduced band gap, reflecting stronger hydrogen-carbon interactions and increased curvature effects. The redistribution of electronic states around the Fermi level confirms enhanced charge transfer and adsorption strength at higher disclination angles, demonstrating that hydrogenation effectively modulates defect states and stabilizes the electronic structure of mono-vacancy CNCs.

Table 3. The configuration structures and the dipole moments of hydrogenated mono-vacancy CNCs, for disclination angles 60˚, 120˚, 180˚, 240˚ and 300˚. The dipole moment is given by Debye.

	Angle 60˚		Angle 120˚		Angle 180˚		Angle 240˚		Angle 300˚	
	Structures	dipole	Structures	dipole	Structures	dipole	Structures	dipole	Structures	dipole
V1	$C_{79}H_{20}$-H^{S1}	7.78	$C_{91}H_{20}$-H^{S1}	9.45	$C_{101}H_{18}$-H^{S1}	11.41	$C_{93}H_{14}$-H^{S1}	12.28	$C_{89}H_{10}$-H^{S1}	24.02
	$C_{79}H_{20}$-H^{S2}	7.68	$C_{91}H_{20}$-H^{S2}	11.11	$C_{101}H_{18}$-H^{S2}	12.96	$C_{93}H_{14}$-H^{S2}	15.74	$C_{89}H_{10}$-H^{S2}	24.21
	$C_{79}H_{20}$-H^{S3}	7.26	$C_{91}H_{20}$-H^{S3}	7.23	$C_{101}H_{18}$-H^{S3}	12.78	$C_{93}H_{14}$-H^{S3}	11.23	$C_{89}H_{10}$-H^{S3}	23.66
V2	$C_{79}H_{20}$-H^{S1}	6.09	$C_{91}H_{20}$-H^{S1}	10.78	$C_{101}H_{18}$-H^{S1}	11.08	$C_{93}H_{14}$-H^{S1}	9.11	$C_{89}H_{10}$-H^{S1}	18.02
	$C_{79}H_{20}$-H^{S2}	6.57	$C_{91}H_{20}$-H^{S2}	9.25	$C_{101}H_{18}$-H^{S2}	10.75	$C_{93}H_{14}$-H^{S2}	10.52	$C_{89}H_{10}$-H^{S2}	22.35
	$C_{79}H_{20}$-H^{S3}	5.42	$C_{91}H_{20}$-H^{S3}	8.75	$C_{101}H_{18}$-H^{S3}	12.83	$C_{93}H_{14}$-H^{S3}	7.85	$C_{89}H_{10}$-H^{S3}	21.86

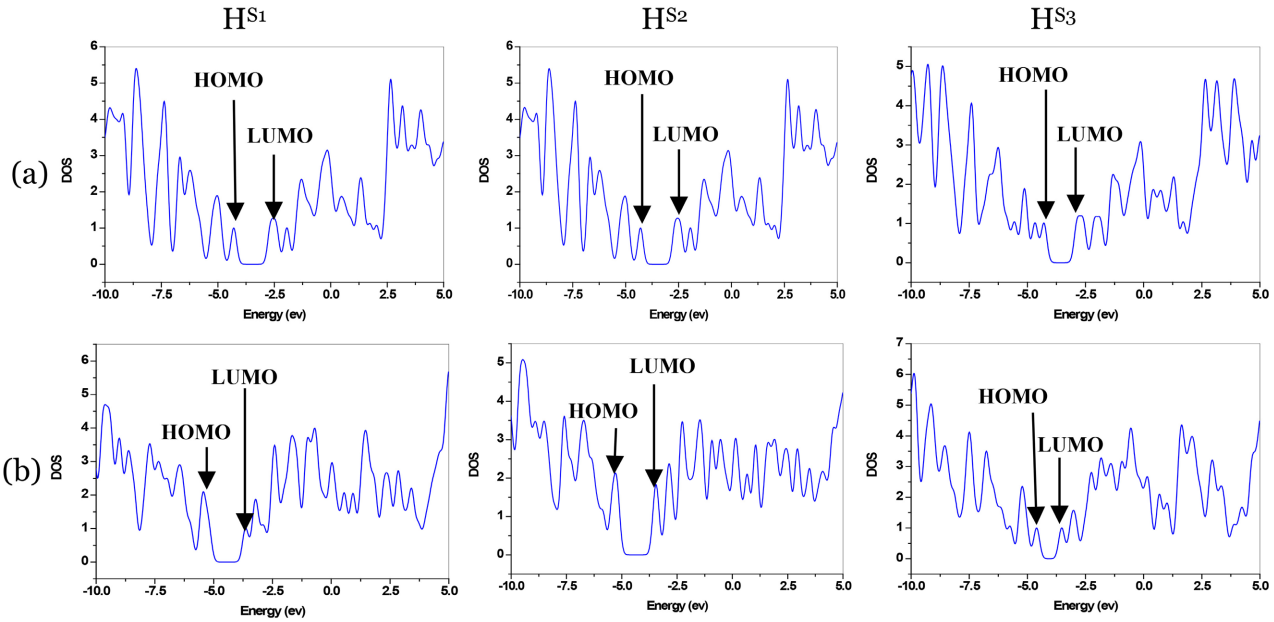

Figure 4. Density of states for hydrogenated mono-vacancy V1 (a) $C_{79}H_{20}$ with disclination angle 60˚ and (b) $C_{89}H_{10}$ with disclination angle 300˚.

3.3. Energy Deposition, Thermal Response, and Vacancy-Induced Localization

The analysis focuses on the HS2 site as it represents the most thermodynamically stable configuration with the strongest adsorption energy, thereby serving as the primary model for evaluating the synergistic effects between DFT energetics and

PHITS irradiation responses. Monte Carlo simulations performed using PHITS 3.35 provide detailed insight into the energy deposition and thermal response of pristine and vacancy-engineered CNC structures listed in Table 4 [41] [46].

Table 4. The configuration structures and the deposited energy, adsorbed dose, irradiation rate and temperature rise of hydrogenated mono-vacancy CNCs, for disclination angles 60˚, 120˚, 180˚, 240˚ and 300˚.

Structures		Deposited Energy ($\times 10^{-9}$ MeV·cm^{-3})		Adsorbed Dose (Gy)		Irradiation Rate (Gy·S^{-1})		ΔT (k)	
		V1	V2	V1	V2	V1	V2	V1	V2
C79H20-60	H^{S1}	0.33	0.27	0.67	0.54	1.8×10^{-3}	1.3×10^{-3}	25.4	17.2
	H^{S2}	0.37	0.31	0.73	0.60	2.0×10^{-3}	1.6×10^{-3}	29.3	20.2
	HS3	0.35	0.29	0.70	0.57	1.9×10^{-3}	1.4×10^{-3}	27.1	18.5
C91H20-120	H^{S1}	0.35	0.29	0.71	0.58	1.9×10^{-3}	1.4×10^{-3}	27.2	18.6
	H^{S2}	0.39	0.33	0.77	0.64	2.1×10^{-3}	1.7×10^{-3}	31.1	21.8
	H^{S3}	0.37	0.31	0.74	0.61	2.0×10^{-3}	1.6×10^{-3}	29.0	20.0
C101H18-180	H^{S1}	0.38	0.32	0.76	0.63	2.1×10^{-3}	1.6×10^{-3}	30.1	21.0
	H^{S2}	0.40	0.34	0.79	0.66	2.2×10^{-3}	1.7×10^{-3}	32.4	22.6
	H^{S3}	0.38	0.32	0.75	0.62	2.1×10^{-3}	1.8×10^{-3}	30.6	21.0
C93H14-240	H^{S1}	0.36	0.30	0.73	0.60	2.0×10^{-3}	1.5×10^{-3}	28.6	19.5
	H^{S2}	0.40	0.34	0.79	0.66	2.2×10^{-3}	1.8×10^{-3}	33.0	22.9
	H^{S3}	0.38	0.32	0.76	0.63	2.1×10^{-3}	1.6×10^{-3}	30.6	21.0
C89H10-300	H^{S1}	0.34	0.28	0.69	0.56	1.9×10^{-3}	1.4×10^{-3}	26.3	18.1
	H^{S2}	0.42	0.36	0.82	0.69	2.3×10^{-3}	1.9×10^{-3}	34.8	24.5
	H^{S3}	0.36	0.30	0.72	0.59	2.0×10^{-3}	1.5×10^{-3}	28.2	19.3

For the pristine CNC, the deposited energy density remains relatively uniform along the carbon framework, with an average of approximately 0.18 - 0.22 MeV/cm^3, reflecting a homogeneous electronic environment. In contrast, vacancy-containing CNCs exhibit pronounced localization of deposited energy around defect sites [52]. Single-vacancy structures show enhanced local energy deposition of approximately ~0.30 MeV/cm^3, a phenomenon that correlates with the structural distortions and electronic redistribution observed in defective carbon systems [53] [54]. The conversion of this energy into thermal energy reveals a corresponding increase in temperature rise (ΔT), which directly reflects localized phonon excitation. As illustrated in Figure 5(a), the localized temperature rise (ΔT) exhibits a linear upward trend with the increase of the disclination angle for both V1 and V2 sites. While the pristine CNC exhibits a modest (ΔT) of approximately 8 - 12 K, single-vacancy systems experience higher temperature increases of ~18 - 22 K. Specifically, the C89H10-V1-HS2 configuration at 300˚ reaches a peak of 34.8 K, whereas the V2 counterpart reaches 24.5 K, indicating that the V1 apex vacancy provides a more efficient environment for phonon confinement. From a practical standpoint, this magnitude of thermal enhancement remains well below the

threshold for carbon framework degradation, yet is sufficiently high to promote thermally assisted hydrogen mobility. The localized ΔT of 34.8 K acts to lower kinetic barriers for hydrogen diffusion and reorientation at adsorption sites, thereby facilitating reversible adsorption-desorption processes without inducing lattice instability.

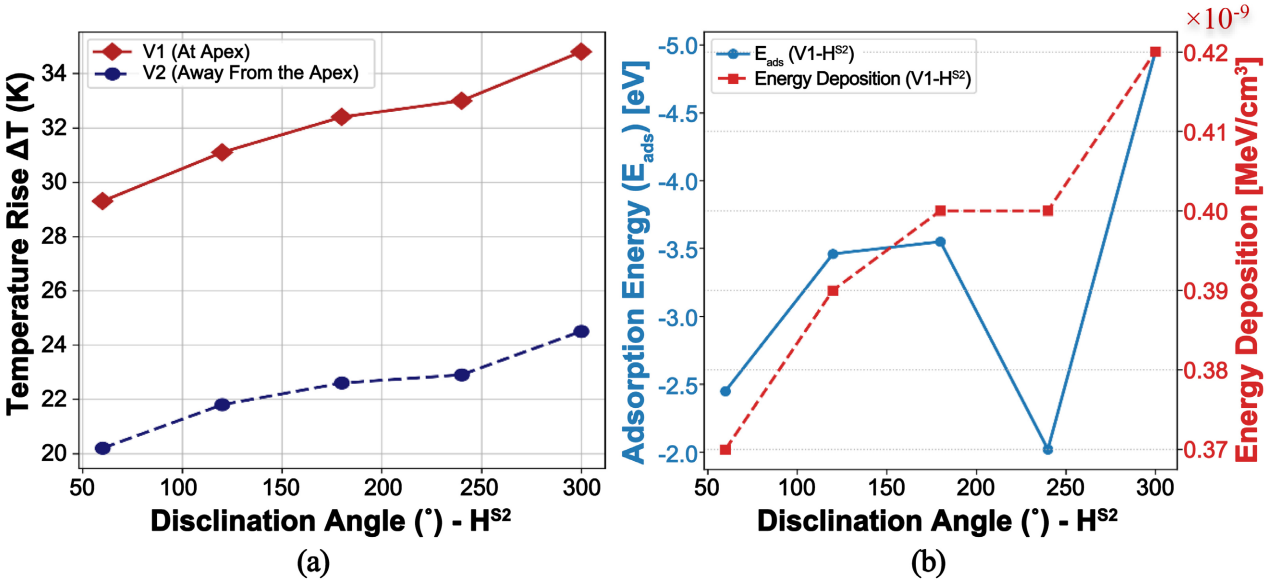

Figure 5. Comprehensive multiscale analysis of the vacancy-engineered CNCs: (a) Localized thermal response (ΔT) across various disclination angles at H^{S2} sites; and (b) Synergistic correlation between DFT-based adsorption energetics and PHITS-simulated energy deposition for the $C_{89}H_{10}$-V1-H^{S2} configuration.

Furthermore, as shown in the synergistic correlation in Figure 5(b), this thermal enhancement is intrinsically linked to thermodynamic stability; the configuration with the highest energy deposition 0.42 MeV/cm³ also exhibits the strongest adsorption energy −4.95 eV. The integration of PHITS 3.35 therefore establishes that structural defects function as controlled "thermal hotspots", enhancing hydrogen activation and transport while preserving the structural integrity of the CNC lattice [55].

3.4. Irradiation Response and Spectral Characteristics of Defective CNCs

The irradiation behavior of CNC structures was further quantified in terms of absorbed dose, irradiation rate, and deposited energy spectra. The pristine CNC exhibits an average absorbed dose of approximately ~0.45 Gy, whereas vacancy-engineered CNCs show significant dose accumulation at defect sites. As compared in Figure 6, single-vacancy configurations display absorbed doses in the range of ~0.60 - 0.65 Gy, while specific configurations reach values up to 0.82 Gy for the V1-H^{S2} site at 300˚. This indicates an increased interaction cross-section resulting from vacancy-induced electronic distortion. Spectral analysis reveals that vacancy-containing structures exhibit broadened energy spectra with extended tails

reaching ~30 - 40 keV, reflecting enhanced secondary electron generation [56]. These irradiation characteristics corroborate DFT-based analyses, which predict increased electronic activity and stronger hydrogen trapping at vacancy sites [57]. And from Table 4, the irradiation rate exhibits a synergistic dependence on both the disclination angle and the localized electronic density induced by vacancy defects. Higher irradiation rates are observed in configurations with larger disclination angle, particularly at the V1 apex site, which correlates directly with the increase energy deposition density and the cumulative absorbed does. Consequently, this combined PHITS-DFT analysis establishes a consistent multiscale interpretation of hydrogen adsorption in vacancy-engineered CNCs. While DFT predicts enhanced hydrogen binding and localized charge accumulation at defect sites, the PHITS simulations confirm that these coordinates act as focal points for energy deposition, thermal excitation, and irradiation-induced enhancement. This synergy demonstrates that vacancy engineering not only optimizes hydrogen adsorption energetics at the atomic scale but also improves macroscopic radiation-energy interaction characteristics, which is critical for real-world hydrogen storage and irradiation-assisted activation processes.

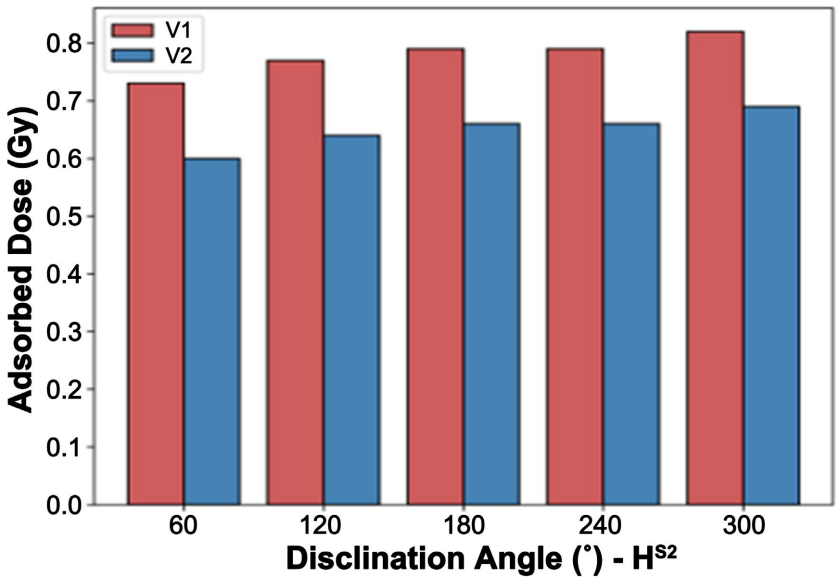

Figure 6. Comparative analysis of the absorbed dose (Gy) across different CNC disclination angles, highlighting the radiation interaction efficiency at V1 and V2 defect sites.

4. Conclusion

The adsorption behavior and electronic properties of carbon nanocones (CNCs) were systematically investigated using a combined DFT and PHITS 3.35 approach. Adsorption energies show a decreasing trend with increasing cone size and disclination angle for hydrogenated mono-vacancy CNCs (V1, V2), with the lowest value of −4.95 eV obtained for $C_{89}H_{10}$-V1-H^{S2}. The smallest energy gap, 0.02 eV, and a maximum dipole moment of 24.21 D were observed for the same system at 300˚. Beyond the atomic-scale analysis, the integration of PHITS 3.35 confirms

that vacancy sites function as macroscopic focal points for energy deposition and localized thermal excitation, peaking at 34.8 K and 0.82 Gy. This synergistic conclusion proves that structural defects not only stabilize hydrogen binding but also enhance the material's interaction with irradiation, providing a robust mechanism for irradiation-assisted hydrogen storage**.** Consequently, mono-vacancy CNCs emerge as highly promising candidates for lightweight and high-efficiency hydrogen storage technologies.

Conflicts of Interest

The authors declare no conflicts of interest regarding the publication of this paper.

References

[1] El-Barbary, A.A., Kamel, M.A., Eid, K.M., Taha, H.O., Mohamed, R.A. and Al-Khateeb, M.A. (2015) The Surface Reactivity of Pure and Monohydrogenated Nanocones Formed from Graphene Sheets. *Graphene*, **4**, 75-83. https://doi.org/10.4236/graphene.2015.44008

[2] El-Barbary, A.A., Kamel, M.A., Eid, K.M., Taha, H.O. and Hassan, M.M. (2015) Mono-Vacancy and B-Doped Defects in Carbon Heterojunction Nanodevices. *Graphene*, **4**, 84-90. https://doi.org/10.4236/graphene.2015.44009

[3] El-Barbary, A.A., Eid, K.M., Kamel, M.A., Taha, H.O. and Ismail, G.H. (2015) Adsorption of CO, CO_2, NO and NO_2 on Boron Nitride Nanotubes: DFT Study. *Journal of Surface Engineered Materials and Advanced Technology*, **5**, 154-161. https://doi.org/10.4236/jsemat.2015.53017

[4] El-Barbary, A.A., Eid, K.M., Kamel, M.A., Taha, H.O. and Ismail, G.H. (2015) Adsorption of CO, CO_2, NO and NO_2 on Carbon Boron Nitride Hetero Junction: DFT Study. *Journal of Surface Engineered Materials and Advanced Technology*, **5**, 169-176. https://doi.org/10.4236/jsemat.2015.54019

[5] EL-Barbary, A.A., Eid, K.M., Kamel, M.A., Osman, H.M. and G. H. Ismail, G.H. (2014) Effect of Tubular Chiralities and Diameters of Single Carbon Nanotubes on Gas Sensing Behavior: A DFT Analysis. *Journal of Surface Engineered Materials and Advanced Technology*, **4**, 66-74. https://doi.org/10.4236/jsemat.2014.42010

[6] EL-Barbary, A.A., Ismail, G.H. and Babeer, A.M. (2013) Effect of Monovacancy Defects on Adsorbing of CO, CO_2, NO and NO_2 on Carbon Nanotubes: First Principle Calculations. *Journal of Surface Engineered Materials and Advanced Technology*, **3**, 287-294. https://doi.org/10.4236/jsemat.2013.34039

[7] Iijima, S. (1991) Helical Microtubules of Graphitic Carbon. *Nature*, **354**, 56-58. https://doi.org/10.1038/354056a0

[8] El-Barbary, A.A., Telling, R.H., Ewels, C.P., Heggie, M.I. and Briddon, P.R. (2003) Structure and Energetics of the Vacancy in Graphite. *Physical Review B*, **68**, Article ID: 144107. https://doi.org/10.1103/physrevb.68.144107

[9] Ewels, C.P., Telling, R.H., El-Barbary, A.A., Heggie, M.I. and Briddon, P.R. (2003) Metastable Frenkel Pair Defect in Graphite: Source of Wigner Energy? *Physical Review Letters*, **91**, Article ID: 025505. https://doi.org/10.1103/physrevlett.91.025505

[10] Telling, R.H., Ewels, C.P., El-Barbary, A.A. and Heggie, M.I. (2003) Wigner Defects Bridge the Graphite Gap. *Nature Materials*, **2**, 333-337. https://doi.org/10.1038/nmat876

[11] Sattler, K. (1995) Scanning Tunneling Microscopy of Carbon Nanotubes and Nanocones. *Carbon*, **33**, 915-920. https://doi.org/10.1016/0008-6223(95)00020-e

[12] Garberg, T., Naess, S.N., Helgesen, G., Knudsen, K.D., Kopstad, G. and Elgsaeter, A. (2008) A Transmission Electron Microscope and Electron Diffraction Study of Carbon Nanodisks. *Carbon*, **46**, 1535-1543. https://doi.org/10.1016/j.carbon.2008.06.044

[13] Heggie, M., Telling, R., El-Barbary, A.A., Suarez-Martinez, I. and Ewels, C. (2004) Carbon under Irradiation-Stiffening, Creeping and Shape Change, Conference: 6. *International Conference on Nano-Technology in Carbon*: *From Synthesis to Applications of Nano-Structured Carbon and Related Materials*, Batz sur Mer, 10-13 October 2004, 48.

[14] El-Barbary, A.A. (2025) IR Spectroscopy Insights and Sensitivity of Fullerene $C_{59}Al$ for Pollutant Gas Detection. *Diamond and Related Materials*, **159**, Article ID: 112738. https://doi.org/10.1016/j.diamond.2025.112738

[15] El-Barbary, A.A., Khurmy, S.M. and Adawi, H. (2025) Band Gap Engineering of Nanocones via Mono-Hydrogenation. *Macromolecular Symposia*, **414**, Article ID: 2400002. https://doi.org/10.1002/masy.202400002

[16] El-Barbary, A.A. (2024) IR Spectroscopic and Vibrational Modes of $C_{59}X$ and $C_{60}X$ Fullerenes (X = Li, Be). *Diamond and Related Materials*, **148**, Article ID: 111448. https://doi.org/10.1016/j.diamond.2024.111448

[17] El-Barbary, A.A. and Adawi, H. (2024) Energetic and Spectroscopic Properties of N-Type and P-Type C_{60} Fullerene. *Diamond and Related Materials*, **147**, Article ID: 111266. https://doi.org/10.1016/j.diamond.2024.111266

[18] EL-Barbary, A.A. and Shabi, A.H. (2024) Stone-Wales Defective C_{60} Fullerene for Hydrogen Storage. *International Journal of Hydrogen Energy*, **71**, 155-164. https://doi.org/10.1016/j.ijhydene.2024.05.240

[19] El-Barbary, A.A. (2023) IR Spectroscopic Analysis of Heterohedral Metallofullerenes. *Diamond and Related Materials*, **136**, Article ID: 110082. https://doi.org/10.1016/j.diamond.2023.110082

[20] Al-Khateeb, M.A. and EL-Barbary, A.A. (2025) Transition-Metal-Enhanced Hydrogen Adsorption on CNNCs: A DFT Analysis. *Middle East Journal of Applied Sciences*, **15**, 179-188. https://www.curresweb.com/index.php/MEJAS1/article/view/645

[21] Alfieri, G. and Kimoto, T. (2009) The Structural and Electronic Properties of Chiral Sic Nanotubes: A Hybrid Density Functional Study. *Nanotechnology*, **20**, Article ID: 285703. https://doi.org/10.1088/0957-4484/20/28/285703

[22] Mavrandonakis, A., Froudakis, G.E., Andriotis, A. and Menon, M. (2006) Silicon Carbide Nanotube Tips: Promising Materials for Atomic Force Microscopy and/or Scanning Tunneling Microscopy. *Applied Physics Letters*, **89**, Article ID: 123126. https://doi.org/10.1063/1.2221418

[23] Zhu, J., Yu, Z., Burkhard, G.F., Hsu, C., Connor, S.T., Xu, Y., *et al.* (2009) Optical Absorption Enhancement in Amorphous Silicon Nanowire and Nanocone Arrays. *Nano Letters*, **9**, 279-282. https://doi.org/10.1021/nl802886y

[24] EL-Barbary, A.A. (2019) Hydrogen Storage on Cross Stacking Nanocones. *International Journal of Hydrogen Energy*, **44**, 20099-20109. https://doi.org/10.1016/j.ijhydene.2019.05.043

[25] El-Barbary, A.A. (2016) Hydrogenated Fullerenes in Space: FT-IR Spectra Analysis. *AIP Conference Proceedings*, **1742**, Article ID: 030005. https://doi.org/10.1063/1.4953126

[26] EL-Barbary, A.A. (2018) Vacancy Cluster in Graphite: Migration Energy and Aggre-

gation Mechanism. *AIP Conference Proceedings*, **1976**, Article ID: 020006. https://doi.org/10.1063/1.5042373

[27] Hindi, A.A. and EL-Barbary, A.A. (2015) Hydrogen Binding Energy of Halogenated C40 Cage: An Intermediate between Physisorption and Chemisorption. *Journal of Molecular Structure*, **1080**, 169-175. https://doi.org/10.1016/j.molstruc.2014.09.034

[28] EL-Barbary, A.A. (2017) New Insights into Canted Spiro Carbon Interstitial in Graphite. *Applied Surface Science*, **426**, 238-243. https://doi.org/10.1016/j.apsusc.2017.07.196

[29] El-Barbary, A.A., Lebda, H.I. and Kamel, M.A. (2009) The High Conductivity of Defect Fullerene C_{40} Cage. *Computational Materials Science*, **46**, 128-132. https://doi.org/10.1016/j.commatsci.2009.02.034

[30] EL-Barbary, A.A. (2016) Hydrogenated Fullerenes Dimer, Peanut and Capsule: An Atomic Comparison. *Applied Surface Science*, **369**, 50-57. https://doi.org/10.1016/j.apsusc.2016.02.033

[31] EL-Barbary, A.A. (2016) Potential Energy of H_2 Inside the C_{116} Fullerene Dimerization: An Atomic Analysis. *Journal of Molecular Structure*, **1112**, 9-13. https://doi.org/10.1016/j.molstruc.2016.02.007

[32] EL-Barbary, A.A. (2016) Hydrogenation Mechanism of Small Fullerene Cages. *International Journal of Hydrogen Energy*, **41**, 375-383. https://doi.org/10.1016/j.ijhydene.2015.10.102

[33] El-Barbary, A.A. (2015) The Surface Reactivity and Electronic Properties of Small Hydrogenation Fullerene Cages. *Journal of Surface Engineered Materials and Advanced Technology*, **5**, 162-168. https://doi.org/10.4236/jsemat.2015.53018

[34] Berry, G.D. and Aceves, S.M. (1998) Onboard Storage Alternatives for Hydrogen Vehicles. *Energy & Fuels*, **12**, 49-55. https://doi.org/10.1021/ef9700947

[35] Chen, P., Wu, X., Lin, J. and Tan, K.L. (1999) High H_2 Uptake by Alkali-Doped Carbon Nanotubes under Ambient Pressure and Moderate Temperatures. *Science*, **285**, 91-93. https://doi.org/10.1126/science.285.5424.91

[36] Liu, C. and Cheng, H. (2005) Carbon Nanotubes for Clean Energy Applications. *Journal of Physics D: Applied Physics*, **38**, R231-R252. https://doi.org/10.1088/0022-3727/38/14/r01

[37] Ströbel, R., Garche, J., Moseley, P.T., Jörissen, L. and Wolf, G. (2006) Hydrogen Storage by Carbon Materials. *Journal of Power Sources*, **159**, 781-801. https://doi.org/10.1016/j.jpowsour.2006.03.047

[38] Baughman, R.H., Zakhidov, A.A. and de Heer, W.A. (2002) Carbon Nanotubes—The Route toward Applications. *Science*, **297**, 787-792. https://doi.org/10.1126/science.1060928

[39] Yang, C., Kanoh, H., Kaneko, K., Yudasaka, M. and Iijima, S. (2002) Adsorption Behaviors of Hipco Single-Walled Carbon Nanotube Aggregates for Alcohol Vapors. *The Journal of Physical Chemistry B*, **106**, 8994-8999. https://doi.org/10.1021/jp025767n

[40] Zhao, Y., Kim, Y., Dillon, A.C., Heben, M.J. and Zhang, S.B. (2005) *Ab Initio* Design of Ca-Decorated Organic Frameworks for High Capacity Molecular Hydrogen Storage with Enhanced Binding. P*hysical Review Letters*, **95**, Article ID: 155504.

[41] Yang, F.H., Lachawiec, A.J. and Yang, R.T. (2006) Adsorption of Spillover Hydrogen Atoms on Single-Wall Carbon Nanotubes. *The Journal of Physical Chemistry B*, **110**, 6236-6244. https://doi.org/10.1021/jp056461u

[42] Sato, T., Iwamoto, Y., Hashimoto, S., Ogawa, T., Furuta, T., Abe, S., *et al.* (2018) Fea-

tures of Particle and Heavy Ion Transport Code System (PHITS) Version 3.02. *Journal of Nuclear Science and Technology*, **55**, 684-690. https://doi.org/10.1080/00223131.2017.1419890

[43] Frisch, M.J., Trucks, G.W., Schlegel, H.B., Scuseria, G.E., Robb, M.A., Cheeseman, J.R., *et al.* (2009) Gaussian 2009. Gaussian Inc.

[44] Becke, A.D. (1993) Density-Functional Thermochemistry. III. The Role of Exact Exchange. *The Journal of Chemical Physics*, **98**, 5648-5652. https://doi.org/10.1063/1.464913

[45] Vosko, S.H. and Wilk, L. (1980) Influence of an Improved Local-Spin-Density Correlation-Energy Functional on the Cohesive Energy of Alkali Metals. *Physical Review B*, **22**, 3812-3815. https://doi.org/10.1103/physrevb.22.3812

[46] Frisch, A., Dennington, R.D., Keith, T.A., Millam, J., Nielsen, A.B., Holder, A.J. and Hiscocks, J. (2003) Gauss View Manual Version 4. Gaussian Inc.

[47] Niita, K., Sato, T., Iwase, H., Nose, H., Nakashima, H. and Sihver, L. (2006) Phits—A Particle and Heavy Ion Transport Code System. *Radiation Measurements*, **41**, 1080-1090. https://doi.org/10.1016/j.radmeas.2006.07.013

[48] El-Barbary, A.A. and Al-Khateeb, M.A. (2018) A Theoretical Study of Hydrogen Adsorption on Surface Nanocone Materials. *Current Science International*, **7**, 370-375.

[49] Ibrahim, M., El-Nahass, M.M., Kamel, M.A., El-Barbary, A.A., Wagner, B.D. and El-Mansy, M.A.M. (2013) On the Spectroscopic Analyses of Thioindigo Dye. *Spectrochimica Acta Part A*: *Molecular and Biomolecular Spectroscopy*, **113**, 332-336. https://doi.org/10.1016/j.saa.2013.05.014

[50] Kotz, J.C., Treichel, P. and Weaver, G.C. (2006) Chemistry and Chemical Reactivity. Thomson Brooks Cole.

[51] Nikitin, A., Li, X., Zhang, Z., Ogasawara, H., Dai, H. and Nilsson, A. (2007) Hydrogen Storage in Carbon Nanotubes through the Formation of Stable C-H Bonds. *Nano Letters*, **8**, 162-167. https://doi.org/10.1021/nl072325k

[52] Ziegler, J.F., Ziegler, M.D. and Biersack, J.P. (2010) SRIM—The Stopping and Range of Ions in Matter (2010). *Nuclear Instruments and Methods in Physics Research Section B*: *Beam Interactions with Materials and Atoms*, **268**, 1818-1823. https://doi.org/10.1016/j.nimb.2010.02.091

[53] Toulemonde, M., Dufour, C. and Paumier, E. (1992) Transient Thermal Process after a High-Energy Heavy-Ion Irradiation of Amorphous Metals and Semiconductors. *Physical Review B*, **46**, 14362-14369. https://doi.org/10.1103/physrevb.46.14362

[54] Szenes, G. (1995) General Features of Latent Track Formation in Magnetic Insulators Irradiated with Swift Heavy Ions. *Physical Review B*, **51**, 8026-8029. https://doi.org/10.1103/physrevb.51.8026

[55] Iwase, H., Niita, K. and Nakamura, T. (2002) Development of General-Purpose Particle and Heavy Ion Transport Monte Carlo Code. *Journal of Nuclear Science and Technology*, **39**, 1142-1151. https://doi.org/10.1080/18811248.2002.9715305

[56] Salvat, F., Fernández-Varea, J.M. and Sempau, J. (2014) PENELOPE: A Code System for Monte Carlo Simulation of Electron and Photon Transport. OECD/NEA Report.

[57] Dingfelder, M., Hantke, D. and Inokuti, M. (2008) Electron Transport and Secondary Electron Production in Condensed Media. *Radiation Physics and Chemistry*, **77**, 1213-1217.